



# Modulating photogenerated electron density of Pr single-atom sites by coordination environment engineering for boosting photoreduction of CO<sub>2</sub> to CH<sub>3</sub>OH

Minzhi Ma<sup>a,b</sup>, Zeai Huang<sup>b</sup>, Lina Li<sup>c</sup>, Wenda Zhang<sup>d</sup>, Rui Guo<sup>b</sup>, Ruiyang Zhang<sup>b</sup>, Wenjun Fa<sup>e</sup>, Chunqiu Han<sup>b</sup>, Yuehan Cao<sup>b</sup>, Shan Yu<sup>b</sup>, Ying Zhou<sup>a,b,\*</sup>

<sup>a</sup> State Key Laboratory of Oil and Gas Reservoir Geology and Exploitation, Southwest Petroleum University, Chengdu 610500, China

<sup>b</sup> School of New Energy and Materials, Southwest Petroleum University, Chengdu 610500, China

<sup>c</sup> Shanghai Synchrotron Radiation Facility (SSRF), Zhangjiang Lab, Shanghai Advanced Research Institute & Shanghai Institute of Applied Physics, Chinese Academy of Sciences, Shanghai 201204, China

<sup>d</sup> Guangxi Key Laboratory of Optic and Electronic Materials and Devices, MOE Key Laboratory of New Processing Technology for Nonferrous Metals and Materials, College of Materials Science and Engineering, Guilin University of Technology, Guilin 541004, China

<sup>e</sup> Key Laboratory of Micro-Nano Materials for Energy Storage and Conversion of Henan Province & College of Advanced Materials and Energy, Xuchang University, Henan, 461000, China

## ARTICLE INFO

### Keywords:

CO<sub>2</sub> to CH<sub>3</sub>OH

Pr single-atom

Coordination environment engineering

Photogenerated electron localization

Ultra-high single-atom loading

## ABSTRACT

The performance of photocatalytic reduction CO<sub>2</sub> to CH<sub>3</sub>OH is intimately tied to the photogenerated electron density of the active center, because CH<sub>3</sub>OH formation involves a 6-electron transfer process. However, the random migration of photocarriers in the photocatalysts is severely not conducive to the directional delivery and enrichment of photogenerated electrons to active sites, leading to poor photocatalytic activity for CO<sub>2</sub> to CH<sub>3</sub>OH. Herein, we reported a coordination environment engineered Pr single-atom catalyst for boosting the photogenerated electron density of the active sites, achieving the high-efficiency photoreduction of CO<sub>2</sub> to CH<sub>3</sub>OH. The carbon nitride (CN) supported Pr single-atom with oxygen coordination was designed via a three-step pyrolysis process. Then, the engineered oxygen coordination configuration for the Pr single-atom (Pr<sub>1</sub>-N<sub>4</sub>O<sub>2</sub>) was successfully achieved. Importantly, this Pr<sub>1</sub>-N<sub>4</sub>O<sub>2</sub> sites can induce photogenerated electrons more easily to accumulate on the Pr atom as compared to the reference catalyst of the Pr atom without oxygen coordination (Pr<sub>1</sub>-N<sub>6</sub>). Moreover, the formed atomically dispersed Pr<sub>1</sub>-N<sub>4</sub>O<sub>2</sub> active centers with ultra-high Pr loading (21.05 wt%) can promote CO<sub>2</sub> adsorption and activation, and provide a high density of active sites for CO<sub>2</sub> photoreduction. As a result, the optimized Pr<sub>1</sub>-N<sub>4</sub>O<sub>2</sub>/CN exhibited a boosted photoreduction of CO<sub>2</sub> to CH<sub>3</sub>OH activity (511.1 μmol g<sup>-1</sup> h<sup>-1</sup>), which was up to 28.9 and 1.9 times higher than those of CN (17.7 μmol g<sup>-1</sup> h<sup>-1</sup>) and Pr<sub>1</sub>-N<sub>6</sub>/CN (274.1 μmol g<sup>-1</sup> h<sup>-1</sup>), and preferable to most reported work under similar catalytic conditions. Our findings can provide a fresh prospect for developing innovative SACs to enhance the photoreduction of CO<sub>2</sub> to CH<sub>3</sub>OH activity.

## 1. Introduction

Converting CO<sub>2</sub> with H<sub>2</sub>O into high value-added chemicals is an appealing way to accomplish carbon neutrality and green-sustainable development [1–3]. Among the CO<sub>2</sub> reduction products, CH<sub>3</sub>OH attracted much attention due to their excellent market price/demand and high energy density [4–7]. For this purpose, emerging photocatalytic CO<sub>2</sub> conversion technology was considered as an elegant solution for CH<sub>3</sub>OH synthesis compared with other strategies [8].

Typically, the catalytic activity of photoreduction of CO<sub>2</sub> to CH<sub>3</sub>OH depends on the amount of electron transfer from the substrate to the active center, because the CH<sub>3</sub>OH generation from CO<sub>2</sub> is a 6-electron transfer reaction [9–12]. This implies that the active center with high photogenerated electron density could significantly elevate the activity of the photocatalysts for the reduction CO<sub>2</sub> to CH<sub>3</sub>OH. However, random photocarrier transfer makes the directional migration of photogenerated electrons very difficult, leading to a lower local photogenerated electron density at active sites [13]. Therefore, achieving the above purpose on

\* Corresponding author at: State Key Laboratory of Oil and Gas Reservoir Geology and Exploitation, Southwest Petroleum University, Chengdu 610500, China.  
E-mail address: [yzhou@swpu.edu.cn](mailto:yzhou@swpu.edu.cn) (Y. Zhou).

<https://doi.org/10.1016/j.apcatb.2023.122626>

Received 30 January 2023; Received in revised form 6 March 2023; Accepted 12 March 2023

Available online 14 March 2023

0926-3373/© 2023 Elsevier B.V. All rights reserved.

the photocatalyst surface is highly demanded to obtain high activity for CH<sub>3</sub>OH generation, but will not be easy to succeed.

Recent studies have indicated that metal single atoms photocatalysts (SACs) with metal-N<sub>x</sub> coordination configuration are attracting increasing attention in the photoreduction of CO<sub>2</sub> [14–16]. Because they are conducive to boosting the directional migration of photogenerated electrons to the metal single-atom to form electron-rich centers [11, 17–20]. In the majority of cases, an atomically dispersed metal-N<sub>x</sub> active site is required to be anchored on the substrate, such as carbon nitride, graphene, or graphene-like carbons [21–23]. These types of substrates generally hold an inherent  $\pi$ -conjugated system [24]. Moreover, the atomically dispersed metal-N<sub>x</sub> active sites can also boost the electrical conductivity of the substrate by the formation of  $d$ - $\pi$  conjugation between the  $d$  orbital of the metal single-atom and the  $\pi$  orbital of the substrate [25–27]. On the positive side, these contribute to accomplishing lower resistance for electron transport in such catalysts and raise the separation efficiency of photogenerated carriers. However, SACs with high electrical conductivity can also lead to easier random migration of photogenerated electrons, restricting the aggregation of photogenerated electrons on the metal-N<sub>x</sub> active site [24]. Therefore, solving this dilemma is crucial for improving the CH<sub>3</sub>OH production activity.

To increase the photogenerated electron density of metal single-atom active sites, sufficient space for storing photogenerated electrons is the primary condition. For achieving this purpose, regulating their coordination environment will be an effective solution to increase the oxidation state of metal atoms [28]. This is because the more positive valence state of the metal element can induce metal single-atom sites to possess more empty orbits for storing photogenerated electrons. On the basis of this consideration, the oxygen element with high electronegativity and environment-friendly is an ideal candidate for regulating the electronic structure of metal sites [29]. Secondly, it is necessary to regulate the migration path of photogenerated electrons for inducing more photogenerated electrons to be directionally transferred to the metal single-atom active sites. Generally, increasing metal single-atom loading can effectively reduce the effective distance migrated for photogenerated electrons from the substrate to the atomically dispersed metal-N<sub>x</sub> active site, resulting in the photogenerated electrons easy to be captured by the metal active sites [30–32]. In addition, it can also attenuate the negative effect of strong  $d$ - $\pi$  conjugation on the localization of photogenerated electrons at metal single-atom sites in the SACs. More importantly, the SACs with high metal loading can provide a higher density of active sites for the photoreduction of CO<sub>2</sub>, which helps to improve photocatalytic activity [14,33]. However, at loading higher than 5.0 wt%, the metal single-atom with high surface energy is commonly prone to migrate and aggregate to clusters [34]. As a result, only a handful of studies could achieve the as-prepared SACs with ultrahigh metal loading ( $\geq 20.0$  wt%) [35–37]. The above considerations indicate that developing an effective strategy to fabricate highly densely populated SACs and manipulating the coordination motif of the metal single-atom by oxygen element might increase the density of photogenerated electrons at the active site. Then, it is likely to boost the performance of photoreduction of CO<sub>2</sub> to CH<sub>3</sub>OH.

As proof of the concept, the CN supported atomically dispersed Pr<sub>1</sub>-N<sub>4</sub>O<sub>2</sub> or Pr<sub>1</sub>-N<sub>6</sub> active sites (Pr<sub>1</sub>-N<sub>4</sub>O<sub>2</sub>/CN, Pr<sub>1</sub>-N<sub>6</sub>/CN) with ultra-high Pr loading photocatalysts were as-prepared to be the desired prototype catalyst. For as-fabricated Pr<sub>1</sub>-N<sub>4</sub>O<sub>2</sub>/CN with Pr loading up to 21.05 wt %, the Pr<sub>1</sub>-N<sub>6</sub>/CN was obtained at first via a two-step calcination induced metal species vaporization strategy and then subjected to oxygen-containing species steam atmosphere. Combined with the AC-HAADF-STEM and the XAS validate that the Pr species were mainly deemed to be single Pr atoms dispersed on the Pr<sub>1</sub>-N<sub>4</sub>O<sub>2</sub>/CN surface, and the first coordination shell of single Pr atom is mainly bonded with four N atoms and two O atoms to form a Pr<sub>1</sub>-N<sub>4</sub>O<sub>2</sub> coordination configuration. In addition, it also found that the preparation strategy of the Pr single-atom catalysts could also be used to prepare Cu, La, and Cr single-

atom photocatalysts, indicating that is a universal strategy for preparing SACs with ultra-high metal loading. Of note, systematical experiments reveal that the O coordination renders a more positive valence state of the Pr single-atom in the Pr<sub>1</sub>-N<sub>4</sub>O<sub>2</sub>/CN photocatalyst compared with the unmodified Pr single-atom in the Pr<sub>1</sub>-N<sub>6</sub>/CN, and then it helps to increase the photogenerated electron density of Pr active site under light irradiation. Apart from that, the Pr single-atom modified by the O atoms can also boost CO<sub>2</sub> adsorption and activation. As a result, the Pr<sub>1</sub>-N<sub>4</sub>O<sub>2</sub>/CN photocatalyst significantly boosted catalytic performance during the photoreduction of CO<sub>2</sub> to produce CH<sub>3</sub>OH.

## 2. Experiments

### 2.1. Materials

All chemical reagents employed in experiments were analytical grade without any further purification. The dicyandiamide, Pr(NO<sub>3</sub>)<sub>3</sub>·6 H<sub>2</sub>O, La(NO<sub>3</sub>)<sub>3</sub>·6 H<sub>2</sub>O, Cu(NO<sub>3</sub>)<sub>2</sub>·3 H<sub>2</sub>O, AgNO<sub>3</sub>, In(NO<sub>3</sub>)<sub>3</sub>·H<sub>2</sub>O, Cd(NO<sub>3</sub>)<sub>2</sub>·4 H<sub>2</sub>O, Ga(NO<sub>3</sub>)<sub>3</sub>·xH<sub>2</sub>O, and Cr(NO<sub>3</sub>)<sub>3</sub>·9 H<sub>2</sub>O were purchased from Aladdin Reagent Co., Ltd. 99% <sup>13</sup>C enriched <sup>13</sup>CO<sub>2</sub> was provided by Chengdu Keyuan Gas Corp.

### 2.2. Synthesis of Pr<sub>1</sub>-N<sub>6</sub>/CN, Pr<sub>1</sub>-N<sub>4</sub>O<sub>2</sub>/CN, and the control samples

The carbon nitride nanosheets (CNNSs) was synthesized by our previously reported work [38]. The CN supported Pr single-atom was fabricated via a facile two-step calcination induced metal species vaporization strategy. In brief, a certain amount of Pr(NO<sub>3</sub>)<sub>3</sub>·6 H<sub>2</sub>O and two grams of CNNSs were mixed with deionized water. After drying on a hot plate, the obtained mixture was put into a semi-closed porcelain boat with a cover. Then, it was heated in a tube furnace to 150 °C within 11 min under Ar flow and kept at this temperature for 9 h. Subsequently, it was heated to 550 °C with a heating rate of 8.67 °C/min, and maintained at this temperature for 1 h. As a result, the Pr atom was anchored on the CN by this strategy. For the reference sample fabrication, such as Cr/CN-0.2, La/CN-0.2, Cu/CN-0.2, Ag/CN-0.2, Cd/CN-0.2, In/CN-0.2, and Ga/CN-0.2, they were as-prepared using the same strategy as described above. La(NO<sub>3</sub>)<sub>3</sub>·6 H<sub>2</sub>O, Cu(NO<sub>3</sub>)<sub>2</sub>·3 H<sub>2</sub>O, AgNO<sub>3</sub>, In(NO<sub>3</sub>)<sub>3</sub>·H<sub>2</sub>O, Cd(NO<sub>3</sub>)<sub>2</sub>·4 H<sub>2</sub>O, Ga(NO<sub>3</sub>)<sub>3</sub>·xH<sub>2</sub>O, and Cr(NO<sub>3</sub>)<sub>3</sub>·9 H<sub>2</sub>O were used as La, Cu, Cr, Ag, Cd, Ga, and In precursors, respectively. Fabricated samples were marked as Metal/CN-x, in which x is the weight ratio of the metal atom to CNNSs. For example, Pr/CN-0.2 means the weight ratio of Pr atom (0.2 g) to CNNSs (1.0 g) of 0.2. Of note, Pr/CN-0.2 was also named Pr<sub>1</sub>-N<sub>6</sub>/CN.

The Pr<sub>1</sub>-N<sub>4</sub>O<sub>2</sub>/CN was prepared using boric acid as the O precursor. In brief, 800 mg of the as-synthesized Pr<sub>1</sub>-N<sub>6</sub>/CN and 2.5 g of boric acid were respectively placed in two ceramic boats. Then, they were heated in a tube furnace to 150 °C within 10 min under Ar flow at 80 mL min<sup>-1</sup> and kept at this temperature for 2 h. Subsequently, they were heated to 300 °C with a heating rate of 10 °C/min, and maintained at this temperature for 1 h. The Cr-O/CN-0.2, La-O/CN-0.2, Cu-O/CN-0.2, Ag-O/CN-0.2, Cd-O/CN-0.2, In-O/CN-0.2, and Ga-O/CN-0.2 were as-prepared using the same strategy with the Pr<sub>1</sub>-N<sub>4</sub>O<sub>2</sub>/CN.

For the reference Pr-S/CN and Pr-P/CN, the preparation method was the same as Pr<sub>1</sub>-N<sub>4</sub>O<sub>2</sub>/CN. Sulfur powder (200.0 mg) and NaH<sub>2</sub>PO<sub>4</sub>·2 H<sub>2</sub>O (200.0 mg) were respectively selected as S and P precursors.

### 2.3. Characterizations

The XRD patterns were obtained by DX-2700B with Cu K $\alpha$  radiation (40 kV, 40 mA). TEM and HR TEM images were conducted by Tecnai G2 F30 electron microscope (200 kV). The XPS patterns were recorded using Thermo ESCALAB250Xi. Of note, all binding energy values were calibrated to the C 1 s level at 284.8 eV. The SEM images of the as-prepared samples were obtained by ZEISS Gemini 300 microscope. The UV-vis curves were obtained by the Shimadzu UV-2600

spectrophotometer and the Ba<sub>2</sub>SO<sub>4</sub> as the reflectance standard. The CO<sub>2</sub> temperature-programmed desorption (TPD) was recorded by AutoChem II 2920 V3.05. The PL patterns were required on a Hitachi F-7000FL. Time-resolved photoluminescence spectra (TR PL) were recorded on FS5 fluorescence lifetime spectrophotometer (Edinburgh, Instruments, UK). FT-IR curves were obtained on Bruker infrared spectrometer (Tensor II) equipped with an MCT detector. Aberration-corrected high-angle annular dark-field scanning transmission electron microscopy (AC-HAADF-STEM) results and the related EDX mapping were conducted on a double-corrected FEI Titan Themis 60–300. ICP-OES result was obtained on an Agilent 730 ICP-OES spectrometer to detect the loading of metal.

The X-ray absorption spectra (XAS) were composed of the X-ray absorption near edge structure (XANES) and extended X-ray absorption fine structure (EXAFS). The Pr-L<sub>3</sub>, Cr-K, Cu-K, and La-L<sub>2</sub> absorption edges of the as-fabricated Pr<sub>1</sub>-N<sub>6</sub>/CN, Pr<sub>1</sub>-N<sub>4</sub>O<sub>2</sub>/CN, Pr<sub>1</sub>-N<sub>4</sub>O<sub>2</sub>/CN-used, Cr/CN-0.2, Cu/CN-0.2, and La/CN-0.2 photocatalysts were acquired at the BL11B beamline of the Shanghai Synchrotron Radiation Facility (SSRF) with transmission mode. In addition, the XAS spectra of the Pr<sub>1</sub>-N<sub>4</sub>O<sub>2</sub>/CN, Pr-P/CN, and Pr-S/CN photocatalysts were obtained by the Rapid XAFS 2 M (Anhui Absorption Spectroscopy Analysis Instrument Co., Ltd.) by transmission mode. All the photocatalysts were diluted with BN before measurements and then pressed into pellets, respectively. All the XAS spectra were normalized and subtracted background with the ATHENA program (uncorrected for the phase shift) [39]. The wavelet transformed (WT) of EXAFS spectra was obtained using the WTEXAFS program [40]. The  $k^3$ -weighted  $\chi(k)$  data in the  $k$ -space ranging from 2.4 to 8.827 Å<sup>-1</sup> (multiplied by a Hanning window function with  $dk = 1.0$  Å<sup>-1</sup>) were Fourier transformed to obtain R space spectra. The coordination structure of the metal single-atom was resolved by the fit of FT EXAFS spectra (R space), the corresponding R-space between 1.3 and 3.0 Å using the ARTEMIS module of IFEFFIT. During the fitting of the FT EXAFS spectra of the as-prepared photocatalysts, the Debye-Waller factor ( $\sigma^2$ ), and energy shift ( $\delta E_0$ ) were allowed to change freely.

## 2.4. Photocatalytic CO<sub>2</sub> reduction experiments

The activity of photocatalytic reduction of CO<sub>2</sub> with H<sub>2</sub>O over the as-prepared photocatalysts was evaluated in a home-designed airtight setup. The detection method of CO<sub>2</sub> reduction activity is consistent with our previous work [10,41]. In brief, 5.0 mg of photocatalysts were evenly spread on the frosted quartz glass at first. Then, it was placed in the reactor and irradiated for 4 h under flowing Ar conditions to eliminate the impurity gas adsorbed on the catalyst surface. For the CO<sub>2</sub> reduction activity test, 4.0 mL of CO<sub>2</sub> and 1.0 mL of H<sub>2</sub>O were injected into the reactor filled with argon. Subsequently, the light was irradiated using a 300 W Xe lamp (Beijing China Education Au-light Co., Ltd., China). The H<sub>2</sub>, CO, and CH<sub>4</sub> were detected using the GC7900 equipped with a TXD-01 column, NCF, TCD, and FID (GC, Tian Mei Analytical Instrument Co., Ltd.). C<sub>x</sub>H<sub>y</sub>O<sub>z</sub> were determined by an Agilent-7890B equipped with an HP/PLOT-Q column and FID (Agilent Technologies Inc., HP/Plot-Q, USA). The CO<sub>2</sub> reduction activity of all photocatalysts was detected at least three times. The <sup>13</sup>CO<sub>2</sub> isotopic experiments were performed on the same method, which was detected by OmniStar GSD-320, Pfeiffer Vacuum.

## 2.5. Photoelectrochemical measurements

The photoelectrochemical characterization was performed on a CHI760E electrochemical workstation (Chenhua Instrument, Shanghai, China) with a three-electrode system. The Ag/AgCl (KCl sat.) was selected as the reference electrode, and Pt wire was used as the counter electrode. The working electrode was as prepared by a doctor blading technique (Binder: ethylcellulose; Basal: FTO; Active surface area: 1 cm<sup>2</sup>), and then it was treated at 120 °C for 3 h. The i-t curve and EIS

Nyquist plots measurements of as-fabricated photocatalysts at open circuit potential (OCP) were conducted in 0.5 M Na<sub>2</sub>SO<sub>4</sub>.

## 2.6. In situ diffuse reflectance infrared Fourier transform spectroscopy (DRIFTS) investigation

The *in-situ* DRIFTS characterization refers to our previously developed method [42,43]. Briefly, 30 mg of the as-fabricated photocatalyst was pretreated at 300 °C for half an hour under a stream of argon gas. Subsequently, the CO<sub>2</sub> with moisture was continuously influx the Har-rick cell reactor. When the adsorption-desorption equilibrium was achieved, the as-prepared photocatalysts were irradiated by a 300 W Xe lamp without gas flow.

# 3. Results and discussion

## 3.1. Synthesis and characterization

The schematic for fabrication of Pr<sub>1</sub>-N<sub>6</sub>/CN and Pr<sub>1</sub>-N<sub>4</sub>O<sub>2</sub>/CN photocatalysts is exhibited in Fig. 1a. The CNNSs is selected as the substrate because it can provide sufficient anchor points for the single Pr atom to lift its loading, which was confirmed in our previous work [38]. Generally, metal nitrate salts with low boiling points (ca. 100 °C) are prone to vaporization at high temperatures when losing crystal water [44–46]. Of note, moisture can induce the migration and aggregation of metal species into larger clusters/particles during high-temperature calcination [47]. These indicate that removing moisture from SACs precursor and selecting metal nitrate salts as the metal single-atom precursor may inhibit the aggregation of metal species during pyrolysis and promote their dispersion. Our highly densely populated Pr<sub>1</sub>-N<sub>6</sub>/CN photocatalyst synthesis process is inspired by mentioned above, therefore, low-temperature annealing (150 °C) is required to remove the moisture or crystal water contained in the Pr<sub>1</sub>-N<sub>6</sub>/CN precursor before the high-temperature process (550 °C). Simultaneously, the Pr(NO<sub>3</sub>)<sub>3</sub>·6 H<sub>2</sub>O was selected as the precursor for the Pr single-atom. So, we define this pyrolysis process as a “two-step calcination induced metal species vaporization strategy”. For the Metal/CN-x synthesis, we took the same strategy as for Pr<sub>1</sub>-N<sub>6</sub>/CN. To modulate the coordination environment of Pr species, we achieve this purpose by heating the oxygen-containing species and Pr<sub>1</sub>-N<sub>6</sub>/CN at 300 °C (Pr<sub>1</sub>-N<sub>4</sub>O<sub>2</sub>/CN), as shown in Fig. 1a.

The XRD pattern of CN exhibits two characteristic diffraction peaks located at 13.3° and 27.4° (Fig. 1b), corresponding to the (100) and (002) planes, respectively [43,48–50]. These could also be observed in the Pr<sub>1</sub>-N<sub>6</sub>/CN and Pr<sub>1</sub>-N<sub>4</sub>O<sub>2</sub>/CN. The FT-IR and XPS spectra are utilized to study the structural skeleton of these as-synthesized samples. As displayed in Fig. S1, the CN, O/CN, Pr<sub>1</sub>-N<sub>6</sub>/CN, and Pr<sub>1</sub>-N<sub>4</sub>O<sub>2</sub>/CN have similar absorption characteristic FT-IR peaks at ca. 1240–1640 and 806 cm<sup>-1</sup>, which were assigned to the carbon-nitrogen heterocycles and the triazine unit, respectively. In addition, two peaks at ~2170 and ~2000 cm<sup>-1</sup> over the Pr<sub>1</sub>-N<sub>6</sub>/CN and Pr<sub>1</sub>-N<sub>4</sub>O<sub>2</sub>/CN were ascribed as the vibration of cyano terminal groups (C≡N) [51]. The basal structural framework composition of the four samples, such as N = C-N, N-(C)<sub>3</sub>, and C=N-C et al., are identical as exhibited in Fig. 1c-d[52]. Furthermore, the binding energies of these peaks for O-CN, Pr<sub>1</sub>-N<sub>6</sub>/CN, and Pr<sub>1</sub>-N<sub>4</sub>O<sub>2</sub>/CN show significant movement compared with the CN (Fig. 1c-d). Based on the analysis presented aforementioned, it can be inferred that the basic structural skeleton of CN is not ruined after the introduction of Pr and/or O atoms into the CN matrix. Moreover, a relatively strong interaction between the Pr atoms and CN was formed.

Of note, no shift of diffraction peaks was observed after the introduction of Pr and/or O atoms into CN matrix, implying that the Pr and/or O atoms were mainly doped on the surface of CN. Impressively, no Pr species are found in the XRD curves of Pr<sub>1</sub>-N<sub>6</sub>/CN and Pr<sub>1</sub>-N<sub>4</sub>O<sub>2</sub>/CN. Likewise, there are no Pr species nanostructures or clusters observed in SEM, TEM, and HR TEM, as shown in Fig. S2. The Pr loading of Pr<sub>1</sub>-N<sub>6</sub>/



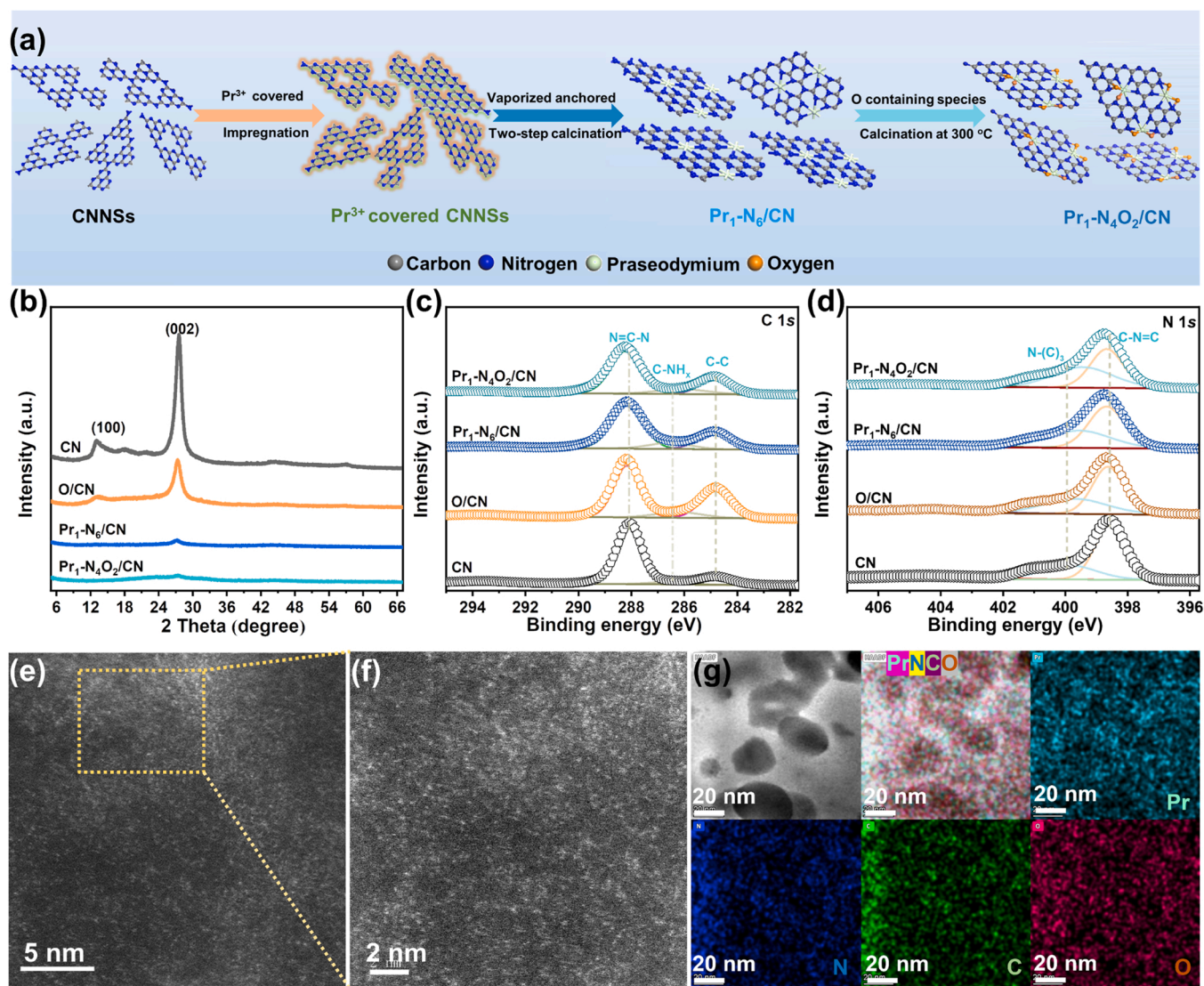


**Fig. 1.** Synthesis process and structural information of the as-fabricated photocatalysts. (a) Schematic of the synthesis process of  $\text{Pr}_1\text{-N}_6/\text{CN}$  and  $\text{Pr}_1\text{-N}_4\text{O}_2/\text{CN}$ ; (b) XRD patterns; High-resolution XPS spectra of (c) C 1s and (d) N 1s over the CN, O/CN,  $\text{Pr}_1\text{-N}_6/\text{CN}$ , and  $\text{Pr}_1\text{-N}_4\text{O}_2/\text{CN}$ ; (e) and (f) AC-HAADF-STEM images, and (g) corresponding EDX mapping images of the as-prepared  $\text{Pr}_1\text{-N}_4\text{O}_2/\text{CN}$ .

CN photocatalyst was detected to be 20.14 wt% by XPS and 24.67 wt% by ICP-OES. The Pr loading of the  $\text{Pr}_1\text{-N}_4\text{O}_2/\text{CN}$  photocatalyst was detected to be 20.34 wt% by XPS and 21.05 wt% by ICP-OES and 20.29 wt% by EDX. These results indicate that the Pr atoms with ultra-high loading may be highly dispersed on the surface of CN substrate in the  $\text{Pr}_1\text{-N}_6/\text{CN}$  and  $\text{Pr}_1\text{-N}_4\text{O}_2/\text{CN}$  photocatalysts.

The AC-HAADF-STEM was used to determine the exact distribution of Pr species on CN surface. As shown in Fig. 1e-f, the isolated bright spots with high density are unambiguously considered as the Pr single-atom on the surface of the  $\text{Pr}_1\text{-N}_4\text{O}_2/\text{CN}$  photocatalyst. Once again, the corresponding EDX mapping further affirms this view (Fig. 1g). These indicate that the Pr species may be exhibited in the atomically dispersed form on the CN substrate surface over the as-prepared  $\text{Pr}_1\text{-N}_4\text{O}_2/\text{CN}$  photocatalyst.

XAS was conducted to discern the electronic structure and coordination mode of Pr atoms on the as-prepared photocatalysts. By the XANES spectra of the Pr  $L_{3\text{-edge}}$  region, the absorption edge position for  $\text{Pr}_1\text{-N}_6/\text{CN}$  and  $\text{Pr}_1\text{-N}_4\text{O}_2/\text{CN}$  is higher than that of  $\text{Pr}_2\text{O}_3$  (Fig. 2a), suggesting that the chemical valance state of Pr in these two photocatalysts is higher than +3. As displayed in Fig. 2b, the oxidation state of Pr in both samples is mainly +4 with a small amount of +3 [53].

Impressively, the Pr  $L_{3\text{-edge}}$  of  $\text{Pr}_1\text{-N}_4\text{O}_2/\text{CN}$  shifts toward higher energy compared with the  $\text{Pr}_1\text{-N}_6/\text{CN}$ , demonstrating that the valance state of Pr in  $\text{Pr}_1\text{-N}_4\text{O}_2/\text{CN}$  is higher than that of  $\text{Pr}_1\text{-N}_6/\text{CN}$  (Fig. 2a). Going even further, the corresponding XPS spectra of Pr 3d can also confirm this view (Fig. 2b). Thus, these XANES and XPS results imply that the Pr atoms on the surface of  $\text{Pr}_1\text{-N}_4\text{O}_2/\text{CN}$  may have more unoccupied orbitals compared with  $\text{Pr}_1\text{-N}_6/\text{CN}$ .

The coordination structure of the Pr atoms on the  $\text{Pr}_1\text{-N}_6/\text{CN}$  and  $\text{Pr}_1\text{-N}_4\text{O}_2/\text{CN}$  photocatalysts was further analyzed by EXAFS and wavelet transform (WT) spectra. As exhibited in Fig. 2c, the FT  $k^3$ -weighted EXAFS (R space) of  $\text{Pr}_1\text{-N}_6/\text{CN}$  and  $\text{Pr}_1\text{-N}_4\text{O}_2/\text{CN}$  exhibits a single major peak, and no Pr-Pr scattering path for metallic Pr species and no Pr-O-Pr scattering path for  $\text{PrO}_x$  species can be detected. It is further confirmed by wavelet transform (WT) analysis. The WT contour plots of the above two photocatalysts display only one maximum peak and the peak position is significantly different from the reference samples (Pr and  $\text{Pr}_2\text{O}_3$ ) (Fig. 2e). Thus, it can draw a conclusion from the XAS and AC-HAADF-STEM analysis results that the Pr species on the  $\text{Pr}_1\text{-N}_6/\text{CN}$  and  $\text{Pr}_1\text{-N}_4\text{O}_2/\text{CN}$  surface are mainly dispersed as Pr single-atom rather than Pr clusters or nanoparticles.

Notably, as displayed in Fig. 2c, the FT-EXAFS spectra of  $\text{Pr}_1\text{-N}_4\text{O}_2/\text{CN}$



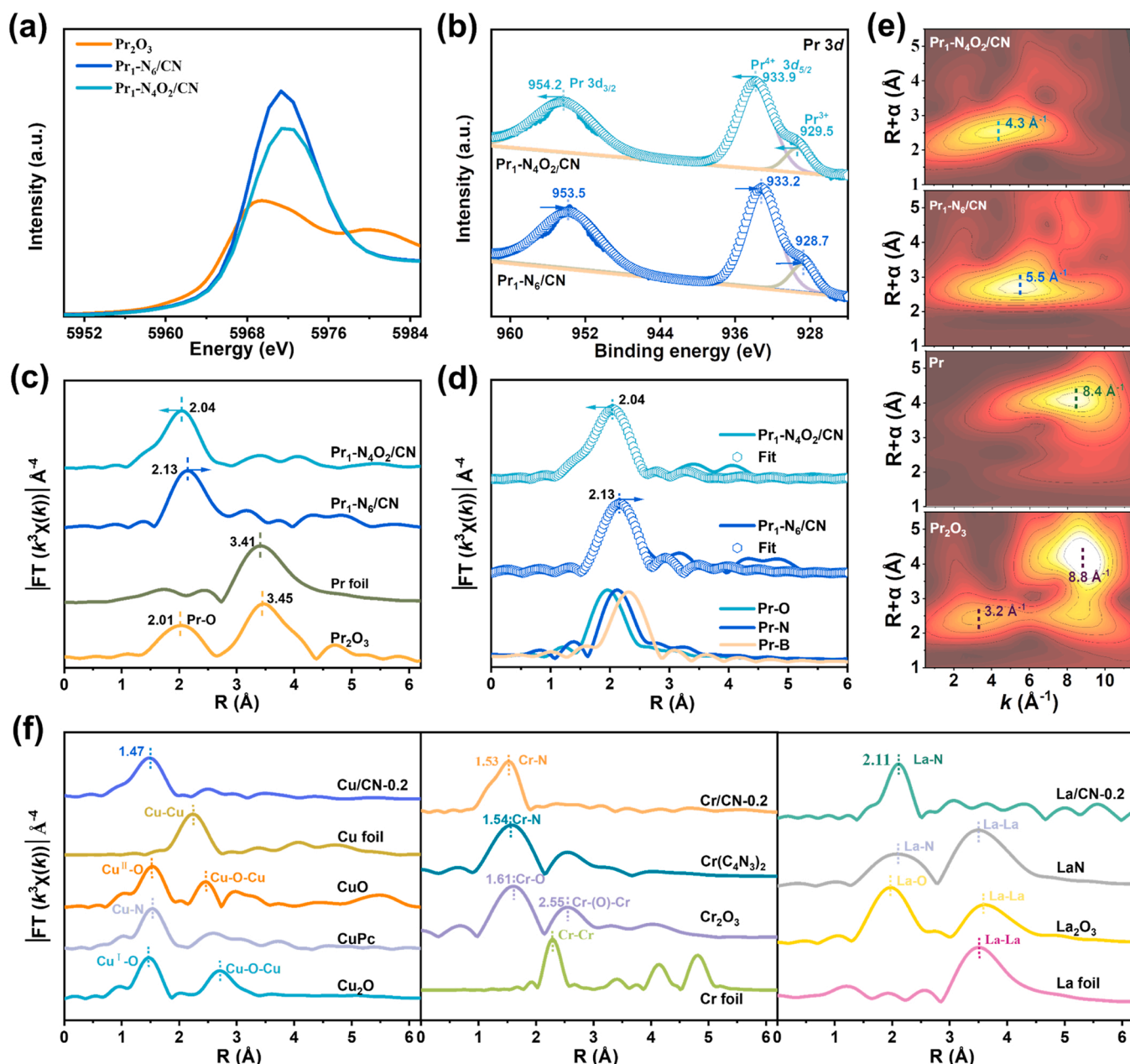


**Fig. 2.** Electronic structure and coordination mode of Pr species in the Pr<sub>1</sub>-N<sub>6</sub>/CN and Pr<sub>1</sub>-N<sub>4</sub>O<sub>2</sub>/CN. (a) Pr L<sub>3</sub>-edge XANES spectra; (b) High-resolution XPS spectra of Pr 3d; (c) FT k<sup>3</sup>-weighted EXAFS spectra (R space) for Pr L<sub>3</sub>-edge; (d) The corresponding EXAFS spectra in R-space fitting curves with the contribution of individual shells; (e) WT plots; (f) FT k<sup>3</sup>-weighted EXAFS spectra for Cu k-edge, Cr k-edge, and La L<sub>2</sub>-edge.

CN present a dominant peak located at 2.04 Å, and it is significantly shifted to the left by 0.09 Å compared with Pr<sub>1</sub>-N<sub>6</sub>/CN (2.13 Å). Moreover, the main peak of Pr<sub>1</sub>-N<sub>4</sub>O<sub>2</sub>/CN is close to the Pr-O scattering path at ca. 2.01 Å, and it is far away from the Pr-B scattering path at ca. 2.30 Å (Fig. 2c and Fig. S3). This indicates that the Pr single-atom on Pr<sub>1</sub>-N<sub>4</sub>O<sub>2</sub>/CN was coordinated with oxygen atoms to form Pr-O bonds rather than coordinated with boron atoms to form Pr-B bonds. The B atom is mainly located in the second shell of the single Pr atom and does not directly bond with Pr [54]. In addition, the WT contour plots of Pr<sub>1</sub>-N<sub>6</sub>/CN and Pr<sub>1</sub>-N<sub>4</sub>O<sub>2</sub>/CN exhibit the same trends and it can further reinforce the above conclusion (Fig. 2e). Moreover, considering that the electronegativity of O element (3.54) is much higher than that of Pr element (1.1). Therefore, it can be concluded that the increase of the Pr single-atom valence state in the Pr<sub>1</sub>-N<sub>4</sub>O<sub>2</sub>/CN photocatalyst is mainly because of the generation of Pr-O bonds compared with the Pr<sub>1</sub>-N<sub>6</sub>/CN photocatalyst. Given that the metal elements tend to coordinate with

unsaturated nitrogen atoms to form metal-N bonds on the carbon nitride substrate [22,55]. Therefore, it can infer that the first shell of single Pr atom on the Pr<sub>1</sub>-N<sub>4</sub>O<sub>2</sub>/CN or Pr<sub>1</sub>-N<sub>6</sub>/CN is mainly composed of nitrogen and oxygen atoms, or nitrogen atoms, respectively.

To acquire the precise coordination configurations of the Pr single-atom in Pr<sub>1</sub>-N<sub>6</sub>/CN and Pr<sub>1</sub>-N<sub>4</sub>O<sub>2</sub>/CN, the corresponding EXAFS curves were fitted in R-space, q-space, and k-space. As shown in Fig. 2d, Fig. S4, and Table S1, the most reasonable fitting results are presented. From the FT EXAFS curves fitting results, the coordination numbers of Pr-N and Pr-O for Pr<sub>1</sub>-N<sub>4</sub>O<sub>2</sub>/CN are 4.0 and 2.3, respectively (Pr-N, 2.64 Å, and Pr-O, 2.42 Å). For the Pr<sub>1</sub>-N<sub>6</sub>/CN, the corresponding coordination number of Pr-N is 6.2 (Pr-N, 2.64 Å). Based on these results, it can conclude that the first coordination shell of single Pr atom on the Pr<sub>1</sub>-N<sub>4</sub>O<sub>2</sub>/CN is mainly bonded with four N atoms (Pr-N bonds) and two O atoms (Pr-O bonds) to form a Pr<sub>1</sub>-N<sub>4</sub>O<sub>2</sub> coordination configuration. For the as-prepared Pr<sub>1</sub>-N<sub>6</sub>/CN, the first coordination shell of single Pr atom

is mainly coupled with six N atoms (Pr-N bonds) to form a  $\text{Pr}_1\text{-N}_6$  coordination configuration. Furthermore, the coordination model of the Pr single-atom over the  $\text{Pr}_1\text{-N}_6/\text{CN}$  and  $\text{Pr}_1\text{-N}_4\text{O}_2/\text{CN}$  is exhibited in Fig. S5.

Interestingly enough, other metal single-atom photocatalysts, represented by copper, chromium, and lanthanum, were also fabricated by the same synthesis method as shown in Fig. 1a. As displayed in Fig. S6, the XRD spectra confirm that no crystallized La or Cu or Cr species are detected, indicating that the La or Cu or Cr species were highly dispersed on the CN matrix. The FT EXAFS spectra of  $\text{Cu}/\text{CN}-0.2$  exhibited a noteworthy Cu-N coordination peak at ca. 1.47 Å, without any apparent Cu-Cu scattering path for metallic Cu species and no Cu-O-Cu scattering path for  $\text{CuO}_x$  species (Fig. 2f and Fig. S7). Meanwhile, no metallic Cr or La and  $\text{CrO}_x$  or  $\text{LaO}_x$  species were observed in the  $\text{Cr}/\text{CN}-0.2$  or  $\text{La}/\text{CN}-0.2$  by the FT EXAS spectra, respectively (Fig. 2f and Fig. S8-9). These XRD and XAS curves analysis results demonstrate that the La, Cu, and Cr species over  $\text{Cu}/\text{CN}-0.2$ ,  $\text{Cr}/\text{CN}-0.2$ , and  $\text{La}/\text{CN}-0.2$  are mainly dispersed as single La, Cu, or Cr atoms, respectively. The Pr (21.05 wt%), Cu (36.05 wt%), La (27.46 wt%), and Cr (24.26 wt%) loading are much higher than that of most previously reported SACs ( $\leq 5.0$  wt%) [35,36].

All in all, the aforementioned results verify that tailoring the electronic structure of Pr single-atom sites is routinely accomplishable via coordination environment engineering, and the synthesis strategy of metal single-atom photocatalysts with ultrahigh loading in our work demonstrates the generality.

### 3.2. Performance evaluation for photocatalytic reduction of $\text{CO}_2$

The photocatalytic activity of the as-fabricated photocatalysts for  $\text{CO}_2$  reduction with  $\text{H}_2\text{O}$  vapor was evaluated in a solid-gas phase batch reactor system without any sacrificial agent and noble metals. As displayed in Fig. 3a, compared with CN, it can be observed that the  $\text{CH}_3\text{OH}$  yield has been increased ca.15.5 times when the atomically dispersed  $\text{Pr}_1\text{-N}_6$  active sites are introduced into CN ( $\text{Pr}_1\text{-N}_6/\text{CN}$ ). Moreover, its  $\text{CH}_3\text{OH}$  generation rate is higher than that of the CN supported different kinds of metal single-atom, and other metallic elements (Fig. 3e-f and Fig. S10). Moreover, Pr has the potential for  $\text{CO}_2$  capture and storage at room temperature [56], which helps to promote the activation and adsorption of  $\text{CO}_2$  in photocatalytic  $\text{CO}_2$  reduction. Based on these

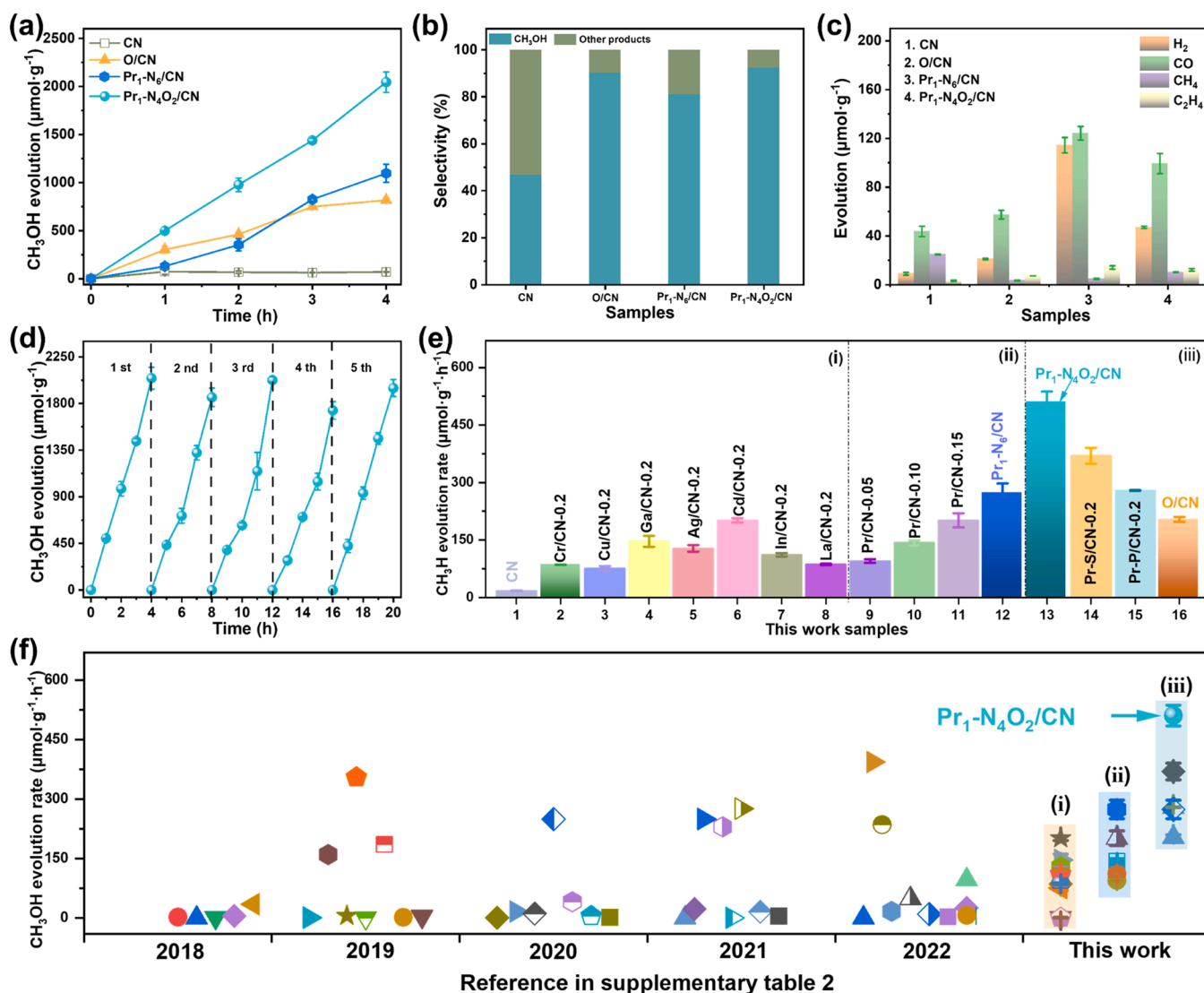


**Fig. 3.** Photocatalytic reduction  $\text{CO}_2$  performance of the as-prepared photocatalysts. (a)  $\text{CH}_3\text{OH}$  production with time for the CN, O/CN,  $\text{Pr}_1\text{-N}_6/\text{CN}$ ,  $\text{Pr}_1\text{-N}_4\text{O}_2/\text{CN}$ ; (b) the selectivity of  $\text{CH}_3\text{OH}$  and other products; (c)  $\text{H}_2$ , CO,  $\text{CH}_4$ , and  $\text{C}_2\text{H}_4$  production in the 4 h; (d)  $\text{CH}_3\text{OH}$  production corresponding to cycle experiments ( $\sim 20$  h) for the  $\text{Pr}_1\text{-N}_4\text{O}_2/\text{CN}$ ; (e)  $\text{CH}_3\text{OH}$  production of the reference photocatalysts synthesized in this work, such as (i) CN supported different kinds of metal elements, (ii) CN supported Pr single-atom with different density, and (iii) CN supported Pr single-atom with different coordination configurations; and (f)  $\text{CH}_3\text{OH}$  evolution rate of various photocatalysts during photocatalytic reduction of  $\text{CO}_2$  with  $\text{H}_2\text{O}$  under the similar reaction conditions over the past five years, for details see [supporting information Table S2](#).

considerations, the Pr was selected as subjects for study in this work.

Notably, it also found that the CH<sub>3</sub>OH production of the Pr<sub>1</sub>-N<sub>6</sub>/CN with ultra-high Pr loading (21.05 wt%) is higher than that of the Pr/CN-x with lower Pr loading (Fig. 3e). This indicates that Pr single-atom active center with high density is essential for boosting the photoreduction of CO<sub>2</sub> to CH<sub>3</sub>OH activity. Impressively, the CH<sub>3</sub>OH yield has been increased ca.1.9 times when the coordination structure of the Pr single-atom on the CN surface is changed from Pr<sub>1</sub>-N<sub>6</sub> to Pr<sub>1</sub>-N<sub>4</sub>O<sub>2</sub>. Overall, the Pr<sub>1</sub>-N<sub>4</sub>O<sub>2</sub>/CN (511.1  $\mu\text{mol g}^{-1} \text{h}^{-1}$ ) photocatalysts displayed excellent CO<sub>2</sub> reduction performance, with CH<sub>3</sub>OH generation rates 28.9, 2.5, and 1.9 times higher than those of CN (17.7  $\mu\text{mol g}^{-1} \text{h}^{-1}$ ), O/CN (204.3  $\mu\text{mol g}^{-1} \text{h}^{-1}$ ), and Pr<sub>1</sub>-N<sub>6</sub>/CN (274.1  $\mu\text{mol g}^{-1} \text{h}^{-1}$ ), respectively. In addition, the CH<sub>3</sub>OH generation rate of the as-prepared Pr<sub>1</sub>-N<sub>4</sub>O<sub>2</sub>/CN sample is higher than most reported work and other as-prepared photocatalysts in this work under similar conditions for reduction CO<sub>2</sub>, as shown in Fig. 3e-f, Fig. S10c, and Table S2. Interestingly, in addition to CH<sub>3</sub>OH, some other by-products, such as H<sub>2</sub>, CO, CH<sub>4</sub>, and C<sub>2</sub>H<sub>4</sub> et. al., were also detected during CO<sub>2</sub> photoreduction (Fig. 3c and Fig. S15b-d). Even then, however, it can be observed that the CH<sub>3</sub>OH selectivity on Pr<sub>1</sub>-N<sub>4</sub>O<sub>2</sub>/CN was very high and reached 92.4%, which is 2.0, 1.02, and 1.1 times higher than that on CN (46.7%),

O/CN (90.2%), and Pr<sub>1</sub>-N<sub>6</sub>/CN (81.0%) as shown in Fig. 3b. These strongly imply that the atomically dispersed Pr<sub>1</sub>-N<sub>4</sub>O<sub>2</sub> active sites with ultra-high loading are critical for photoreduction of CO<sub>2</sub> via H<sub>2</sub>O to CH<sub>3</sub>OH with high activity and selectivity. More importantly, as displayed in Fig. S10c, it can be found that the CH<sub>3</sub>OH yield shows a significant increase trend after the coordination of metal elements with oxygen atoms. These results suggest that it is a general strategy to use oxygen atoms to regulate the coordination environment of metal atoms to enhance its photocatalytic reduction activity of CO<sub>2</sub> to CH<sub>3</sub>OH.

Durability of the Pr<sub>1</sub>-N<sub>4</sub>O<sub>2</sub>/CN was determined by reusing the photocatalyst 5 times (~20 h). As shown in Fig. 3d and Fig. S12a, the yield and selectivity of CH<sub>3</sub>OH for Pr<sub>1</sub>-N<sub>4</sub>O<sub>2</sub>/CN were stable without apparent deactivation. Moreover, for the by-products, as exhibited in Fig. S12b, no significant decrease in the generation rate was observed. These suggest that Pr<sub>1</sub>-N<sub>4</sub>O<sub>2</sub>/CN presented excellent durability for CH<sub>3</sub>OH synthesis from CO<sub>2</sub> photoreduction. The XAS and XPS spectra demonstrated that the electronic structure and coordination structure (Pr<sub>1</sub>-N<sub>4</sub>O<sub>2</sub>) of the Pr single-atom in the Pr<sub>1</sub>-N<sub>4</sub>O<sub>2</sub>/CN exhibited no obvious change after 5 cycles (~20 h), as shown in Figs. S13-14. Moreover, the XAS spectra demonstrate that the Pr atoms atomically dispersed on Pr<sub>1</sub>-N<sub>4</sub>O<sub>2</sub>/CN-used with no agglomeration (Fig. S14).

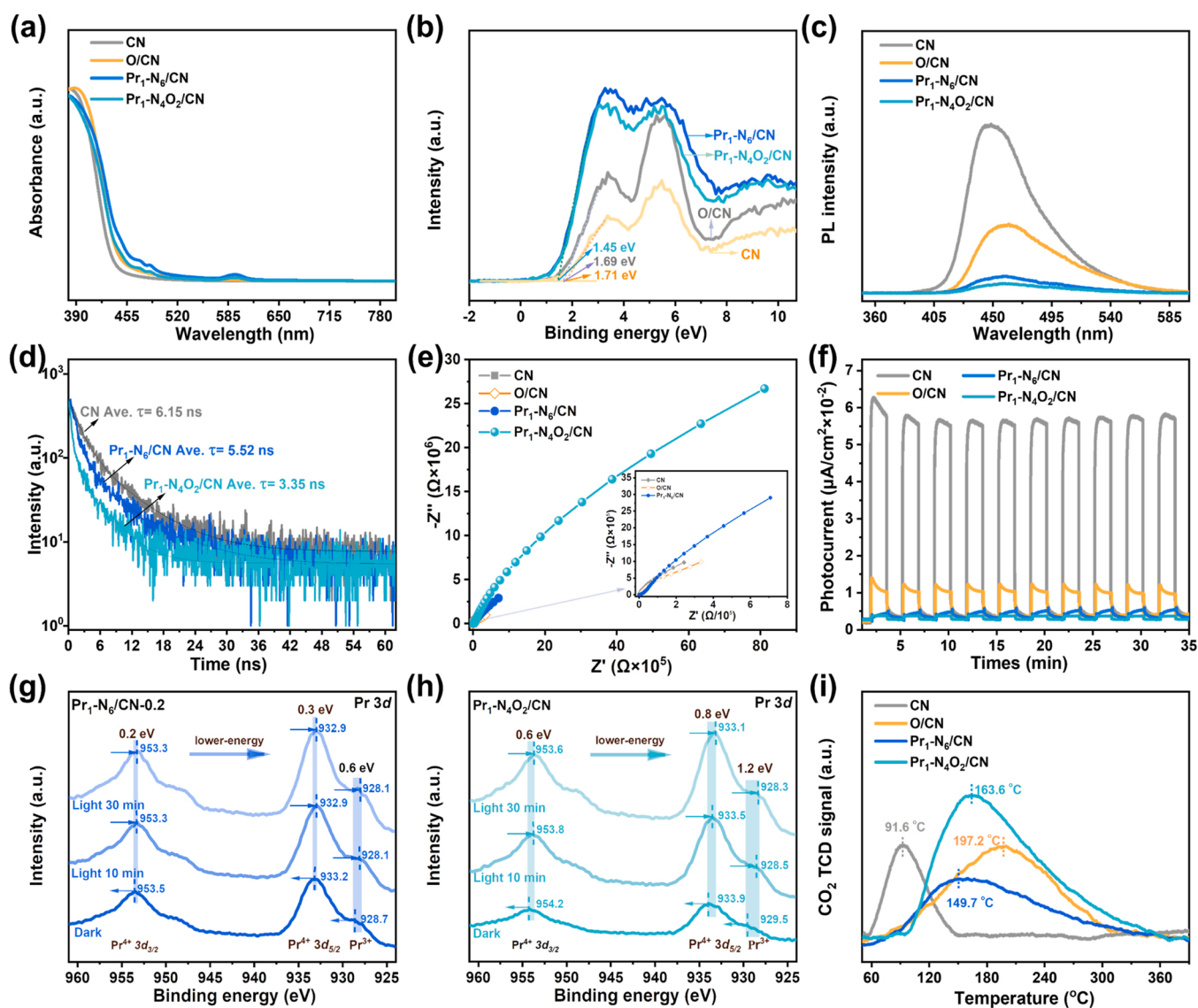


**Fig. 4.** Effect of the electronic structure of single Pr atom on photogenerated carriers density. (a) UV-vis; (b) XPS valence spectra; (c) PL spectra; (d) TR PL spectra; (e) EIS Nyquist plots under dark conditions; (f) i-t curves; Pr 3d XPS spectra of (g) Pr<sub>1</sub>-N<sub>6</sub>/CN and (h) Pr<sub>1</sub>-N<sub>4</sub>O<sub>2</sub>/CN in the dark or light; (i) CO<sub>2</sub> TPD.



Therefore, it can infer that the stable photocatalytic activity for CH<sub>3</sub>OH synthesis from CO<sub>2</sub> photoreduction may be because of the good structural stability over the Pr<sub>1</sub>-N<sub>4</sub>O<sub>2</sub>/CN. The control experiments exhibited that no products were determined by the lack of CO<sub>2</sub> or H<sub>2</sub>O or light or photocatalysts. It suggests that the formed CH<sub>3</sub>OH mainly originated from the CO<sub>2</sub> photoreduction, and the <sup>13</sup>CO<sub>2</sub> labeling experiments also confirmed this view as displayed in Fig. S15a. All in all, it can be concluded that the Pr single-atom with Pr<sub>1</sub>-N<sub>4</sub>O<sub>2</sub> coordination configuration and ultra-high loading played an important role in improving the photocatalytic reduction of CO<sub>2</sub> to CH<sub>3</sub>OH activity.

### 3.3. Mechanism of enhancing CH<sub>3</sub>OH production via the coordination environment engineering

To shed light on the origin of improved photoreduction of CO<sub>2</sub> to CH<sub>3</sub>OH activity, three factors are considered, such as (i) light adsorption, (ii) photogenerated carriers separation and migration, and (iii) surface reaction. The absorption edge of the four samples is similar, indicating that the improved photocatalytic performance of Pr<sub>1</sub>-N<sub>4</sub>O<sub>2</sub>/CN could not ascribe to the light absorption (Fig. 4a). The weak absorption at around 585 nm over the Pr<sub>1</sub>-N<sub>6</sub>/CN and Pr<sub>1</sub>-N<sub>4</sub>O<sub>2</sub>/CN was ascribed to the characteristic transition of Pr<sup>3+</sup> <sup>1</sup>D<sub>2</sub> → <sup>3</sup>H<sub>4</sub> [57,58]. In addition, as exhibited in Fig. 4b and Figs. S16–17, it can observe that the band structure of the Pr<sub>1</sub>-N<sub>4</sub>O<sub>2</sub>/CN and corresponding reference samples can meet the demands of photoreduction of CO<sub>2</sub> with H<sub>2</sub>O to CH<sub>3</sub>OH.

The photocarrier separation and migration over Pr<sub>1</sub>-N<sub>4</sub>O<sub>2</sub>/CN and the reference were investigated by combining the analysis of PL, TR PL, EIS plots, i-t curves, and XPS spectra of the Pr 3d under light conditions. The sharply decreasing PL peak occurs on the Pr<sub>1</sub>-N<sub>4</sub>O<sub>2</sub>/CN relative to Pr<sub>1</sub>-N<sub>6</sub>/CN, O/CN, and CN, implying that intrinsic radiative recombination is significantly inhibited by the introduction of Pr single-atom with O coordination (Fig. 4c). The TR PL decay spectra discover that the average radiative lifetimes of CN, Pr<sub>1</sub>-N<sub>6</sub>/CN, and Pr<sub>1</sub>-N<sub>4</sub>O<sub>2</sub>/CN was 6.15, 5.52, and 3.35 ns, respectively (Fig. 4d). This significantly reduced exciton lifetime demonstrates that the Pr single-atom with oxygen atom coordination accelerates the transfer of electrons from CN to the single Pr atoms active sites [59]. EIS impedance is usually used to study the ease of electron transport in catalytic materials [60]. Of note, the Pr<sub>1</sub>-N<sub>4</sub>O<sub>2</sub>/CN demonstrates the highest ESI impedance (Fig. 4e), and lowest photocurrent (Fig. 4f) compared with the CN, O/CN, and Pr<sub>1</sub>-N<sub>6</sub>/CN, indicating that the random migration of photogenerated electrons on the Pr<sub>1</sub>-N<sub>4</sub>O<sub>2</sub>/CN photocatalyst is greatly restricted. Therefore, we can speculate that this may contribute to the aggregation of photogenerated electrons at the atomically dispersed Pr<sub>1</sub>-N<sub>4</sub>O<sub>2</sub> sites. To verify this notion, the quasi *in-situ* XPS measurements were used to investigate the distribution of the photogenerated electrons under light irradiation. For the Pr<sub>1</sub>-N<sub>6</sub>/CN, it can be observed that all peaks shifted toward lower binding energy by 0.2–0.6 eV under light irradiation as shown in Fig. 4g. This indicates that the Pr single-atom sites on the Pr<sub>1</sub>-N<sub>6</sub>/CN are prone to enrich photogenerated electrons to form photogenerated electron localization centers under illumination. Strikingly, all peaks shifted toward lower binding energy by 0.6–1.2 eV under light irradiation when the coordination mode of the Pr single-atom changes from Pr<sub>1</sub>-N<sub>6</sub> to Pr<sub>1</sub>-N<sub>4</sub>O<sub>2</sub> (Fig. 4h). These demonstrate that the photogenerated electron density of Pr single-atom on the Pr<sub>1</sub>-N<sub>4</sub>O<sub>2</sub>/CN is more than twice that of Pr<sub>1</sub>-N<sub>6</sub>/CN under light irradiation. Thus, it could be concluded that boosting the valance state of Pr single-atom by oxygen coordination can drive photogenerated electrons to accumulate on atomically dispersed Pr<sub>1</sub>-N<sub>4</sub>O<sub>2</sub> sites. Subsequently, the Pr<sub>1</sub>-N<sub>4</sub>O<sub>2</sub> sites could boost the activity of photoreduction of CO<sub>2</sub> to CH<sub>3</sub>OH. The control experiments further confirmed this notion. As shown in Fig. S18, when the P (2.19) or S (2.58) element with lower electronegativity coordinated with the Pr single-atom, its corresponding oxidation state was smaller than that of the Pr single-atom coordinated with oxygen. Eventually, the activity of photocatalytic reduction of CO<sub>2</sub> to CH<sub>3</sub>OH over the Pr-P/CN and Pr-S/CN is lower than that of Pr<sub>1</sub>-N<sub>4</sub>O<sub>2</sub>/CN

(Fig. 3e). All in all, these means that improving the oxidation state of highly densely populated Pr single-atom with oxygen coordination plays a crucial role in increasing the activity of CH<sub>3</sub>OH generation.

To investigate the surface reaction process, the CO<sub>2</sub> TPD and *in situ* DRIFTS were conducted. As displayed in Fig. 4i, the adsorption amount of CO<sub>2</sub> on Pr<sub>1</sub>-N<sub>4</sub>O<sub>2</sub>/CN (887.2 μmol g<sup>-1</sup>) was 12.6, 1.4, and 2.1 times higher than those of CN (70.4 μmol g<sup>-1</sup>), O/CN (622.1 μmol g<sup>-1</sup>), and Pr<sub>1</sub>-N<sub>6</sub>/CN (421.2 μmol g<sup>-1</sup>). This indicates that the atomically dispersed Pr<sub>1</sub>-N<sub>4</sub>O<sub>2</sub> sites significantly boost the adsorption capacity of CO<sub>2</sub>. More importantly, the adsorption strength of CO<sub>2</sub> on Pr<sub>1</sub>-N<sub>4</sub>O<sub>2</sub>/CN (163.6 °C) was higher than that on CN (91.6 °C) and Pr<sub>1</sub>-N<sub>6</sub>/CN (149.7 °C), respectively. It indicates that the Pr<sub>1</sub>-N<sub>4</sub>O<sub>2</sub> species showed a higher ability to activate CO<sub>2</sub> molecules than that of CN and Pr<sub>1</sub>-N<sub>6</sub>/CN. All in all, it can be concluded that manipulating the coordination mode of Pr single-atom by O atoms can significantly facilitate CO<sub>2</sub> adsorption and activation.

Subsequently, the *in-situ* DRIFTS was used to track the reaction intermediates during photoreduction of CO<sub>2</sub> by H<sub>2</sub>O on the surface of Pr<sub>1</sub>-N<sub>6</sub>/CN and Pr<sub>1</sub>-N<sub>4</sub>O<sub>2</sub>/CN under light irradiation. The intensity of the infrared peaks at 1694 cm<sup>-1</sup> (HCO<sub>3</sub><sup>-</sup>), 1650 cm<sup>-1</sup> (HCO<sub>3</sub><sup>-</sup>), 1551 cm<sup>-1</sup> (b-CO<sub>3</sub><sup>2-</sup>), 1472 cm<sup>-1</sup> (m-CO<sub>3</sub><sup>2-</sup>), 1381 cm<sup>-1</sup> (m-CO<sub>3</sub><sup>2-</sup>), 1088 cm<sup>-1</sup> (m-CO<sub>3</sub><sup>2-</sup>), and 920/860 cm<sup>-1</sup> (CO<sub>3</sub><sup>2-</sup>) exhibit a continuously increasing trend over time (Fig. 5a and 5c) [61–65]. These were generally deemed as the crucial CO<sub>2</sub>-related adsorbed intermediates species. It indicates that the atomically dispersed Pr<sub>1</sub>-N<sub>6</sub> and Pr<sub>1</sub>-N<sub>4</sub>O<sub>2</sub> active sites can achieve both CO<sub>2</sub> adsorption and activation, which is one of the prerequisites for photocatalytic reduction of CO<sub>2</sub>. Of note, new absorption peaks at 1705 cm<sup>-1</sup> (HCOOH), 1103 cm<sup>-1</sup> (CH<sub>3</sub>O\*), and 1048 cm<sup>-1</sup> (CH<sub>3</sub>O\*) could be discerned (Figs. 5b and 5d) [61,66–69], which were identified as the crucial intermediates for the CH<sub>3</sub>OH generation [70–72]. More importantly, the intensity of these peaks increases with prolonged illumination time. These indicate that the atomically dispersed Pr<sub>1</sub>-N<sub>6</sub> and Pr<sub>1</sub>-N<sub>4</sub>O<sub>2</sub> active sites can effectively convert CO<sub>2</sub> into key intermediate products necessary for CH<sub>3</sub>OH generation.

Therefore, compared with the Pr<sub>1</sub>-N<sub>6</sub>/CN, the Pr<sub>1</sub>-N<sub>4</sub>O<sub>2</sub>/CN can achieve the efficient photoreduction of CO<sub>2</sub> to CH<sub>3</sub>OH mainly because of the following three points. (i) modulating the electronic structure of the single Pr atom with oxygen atom can directionally induce the photo-generated electrons to enrich on Pr single-atom sites under light illumination (Scheme 1); (ii) then it can significantly facilitate CO<sub>2</sub> adsorption and activation, which can contribute to the photocatalytic reduction of CO<sub>2</sub> to CH<sub>3</sub>OH. (iii) the atomically dispersed Pr<sub>1</sub>-N<sub>4</sub>O<sub>2</sub> sites with ultra-high loading can provide many active sites for CO<sub>2</sub> reduction. As a result, it can conclude that modulating the coordination environment of the metal active sites by oxygen atoms could boost the activity of photocatalytic reduction of CO<sub>2</sub> to CH<sub>3</sub>OH.

## 4. Conclusion

In conclusion, we have successfully developed a novel and universal strategy for fabricating metal single-atom photocatalysts with ultra-high loading. More importantly, rendering a more positive valence state of the Pr element by oxygen coordination could drive the photogenerated electrons to enrich the Pr single-atom active sites under light irradiation. Moreover, the formed atomically dispersed Pr<sub>1</sub>-N<sub>4</sub>O<sub>2</sub> sites with ultra-high density (21.05 wt%) can support ample CO<sub>2</sub> reduction active sites and promote the adsorption and activation of CO<sub>2</sub>. As a result, the CH<sub>3</sub>OH generation rate of the Pr<sub>1</sub>-N<sub>4</sub>O<sub>2</sub>/CN (511.1 μmol g<sup>-1</sup> h<sup>-1</sup>) manifests 28.9 and 1.9 times higher than those of CN (17.7 μmol g<sup>-1</sup> h<sup>-1</sup>) and Pr<sub>1</sub>-N<sub>6</sub>/CN (274.1 μmol g<sup>-1</sup> h<sup>-1</sup>). Our work can enlighten the further designing of promising photocatalysts for the efficient photoreduction of CO<sub>2</sub> to CH<sub>3</sub>OH, which was based on the modulating coordination mode of highly densely populated metal single-atom by the oxygen atoms.

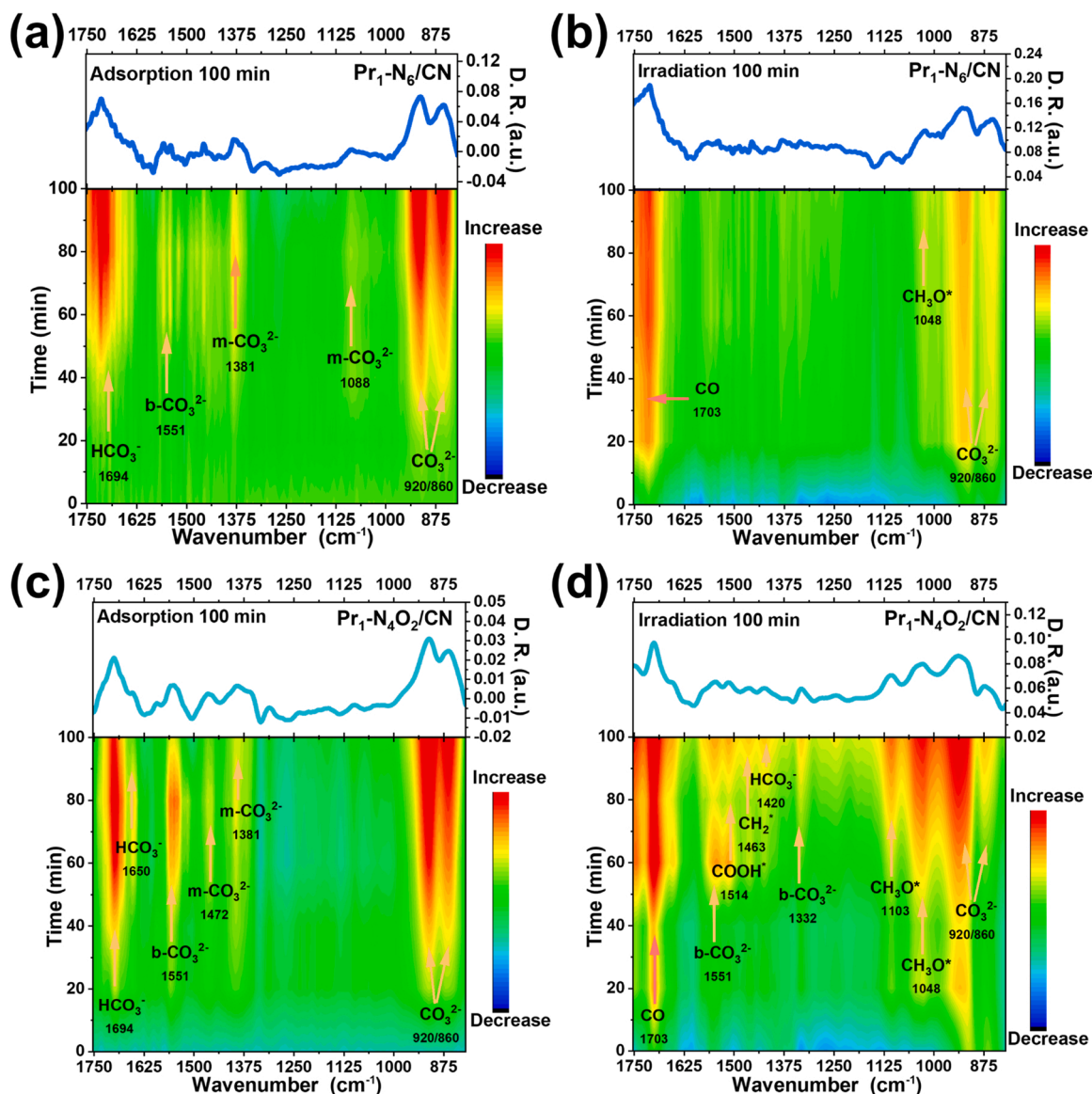
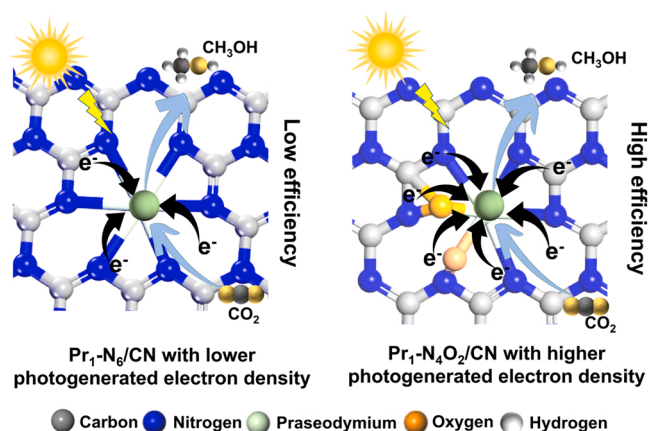


Fig. 5. *In situ* DRIFTS spectra of photoreduction of  $\text{CO}_2$  with  $\text{H}_2\text{O}$  over the  $\text{Pr}_1\text{-N}_6/\text{CN}$  and  $\text{Pr}_1\text{-N}_4\text{O}_2/\text{CN}$ . (a, c)  $\text{CO}_2$  adsorption under dark and (b, d)  $\text{CO}_2$  reduction process under light irradiation.



Scheme 1. Photocatalytic mechanism. Illustration of atomically dispersed  $\text{Pr}_1\text{-N}_4\text{O}_2$  active sites with high photogenerated electron density to boost photoreduction of  $\text{CO}_2$  to  $\text{CH}_3\text{OH}$  activity.

#### CRediT authorship contribution statement

Minzhi Ma, and Ying Zhou designed the study. Zeai Huang, Lina Li, Wenjun Fa, and Ying Zhou provided the support on experimental feasibility. Minzhi Ma, Zeai Huang, Lina Li, Wenda Zhang, Rui Guo, Ruiyang Zhang, Wenjun Fa, Chunqiu Han, Yuehan Cao, Shan Yu, and Ying Zhou, performed characterization and analysis under the supervision of Ying Zhou. Minzhi Ma wrote the paper. Zeai Huang, and Ying Zhou revised the paper. All authors contributed to the interpretation of the results and improvement of the paper.

#### Declaration of Competing Interest

The authors declare that they have no known competing financial interests or personal relationships that could have appeared to influence the work reported in this paper.

#### Data Availability

Data will be made available on request.

## Acknowledgments

We acknowledge the financial supported by Natural Science Foundation of China (No. 22211530070, 22209136, 22209135), Sichuan Science and Technology Program (No. 2021YFH0055, 2022YFH0084, 2022YFSY0050), Natural Science Foundation of Sichuan (2022NSFSC1264). Special Project for the Central Government to Guide the Development of Local Science and Technology in Sichuan Province (No. 22ZYZTS0231), China Postdoctoral Science Foundation (No. 2022M722635). We acknowledge the BL11B beamline of the Shanghai Synchrotron Radiation Facility (SSRF).

## Appendix A. Supporting information

Supplementary data associated with this article can be found in the online version at [doi:10.1016/j.apcatb.2023.122626](https://doi.org/10.1016/j.apcatb.2023.122626).

## References

- [1] Y.S. Zhou, Z.T. Wang, L. Huang, S. Zaman, K. Lei, T. Yue, Z.A. Li, B. You, B.Y. Xia, Engineering 2D photocatalysts toward carbon dioxide reduction, *Adv. Energy Mater.* 11 (2021) 2003159.
- [2] G. Zhang, T. Wang, M. Zhang, L. Li, D. Cheng, S. Zhen, Y. Wang, J. Qin, Z.J. Zhao, J. Gong, Selective CO<sub>2</sub> electroreduction to methanol via enhanced oxygen bonding, *Nat. Commun.* 13 (2022) 7768.
- [3] Y. Xing, X. Wang, S. Hao, X. Zhang, X. Wang, W. Ma, G. Zhao, X. Xu, Recent advances in the improvement of g-C<sub>3</sub>N<sub>4</sub> based photocatalytic materials, *Chin. Chem. Lett.* 32 (2021) 13–20.
- [4] Y. Wang, E. Chen, J. Tang, Insight on reaction pathways of photocatalytic CO<sub>2</sub> conversion, *ACS Catal.* 12 (2022) 7300–7316.
- [5] Y. Wang, R. Godin, J.R. Durrant, J. Tang, Efficient hole trapping in carbon dot/oxygen-modified carbon nitride heterojunction photocatalysts for enhanced methanol production from CO<sub>2</sub> under neutral conditions, *Angew. Chem. Int. Ed.* 60 (2021) 20811–20816.
- [6] Y. Wang, X. Liu, X. Han, R. Godin, J. Chen, W. Zhou, C. Jiang, J.F. Thompson, K. B. Mustafa, S.A. Shevlin, J.R. Durrant, Z. Guo, J. Tang, Unique hole-accepting carbon-dots promoting selective carbon dioxide reduction nearly 100% to methanol by pure water, *Nat. Commun.* 11 (2020) 2531.
- [7] V. Hasija, A. Kumar, A. Sudhaik, P. Raizada, P. Singh, Q. Van, L.T. Le, V.-H. Nguyen, Step-scheme heterojunction photocatalysts for solar energy, water splitting, CO<sub>2</sub> conversion, and bacterial inactivation: a review, *Environ. Chem. Lett.* 19 (2021) 2941–2966.
- [8] Y.A. Wu, I. McNulty, C. Liu, K.C. Lau, Q. Liu, A.P. Paulikas, C.-J. Sun, Z. Cai, J. R. Guest, Y. Ren, V. Stamenkovic, L.A. Curtiss, Y. Liu, T. Rajh, Facet-dependent active sites of a single Cu<sub>2</sub>O particle photocatalyst for CO<sub>2</sub> reduction to methanol, *Nat. Energy* 4 (2019) 957–968.
- [9] X.D. Li, Y.F. Sun, J.Q. Xu, Y.J. Shao, J. Wu, X.L. Xu, Y. Pan, H.X. Ju, J.F. Zhu, Y. Xie, Selective visible-light-driven photocatalytic CO<sub>2</sub> reduction to CH<sub>4</sub> mediated by atomically thin CuIn<sub>5</sub>S<sub>8</sub> layers, *Nat. Energy* 4 (2019) 690–699.
- [10] Y. Cao, L. Guo, M. Dan, D.E. Doronkin, C. Han, Z. Rao, Y. Liu, J. Meng, Z. Huang, K. Zheng, P. Chen, F. Dong, Y. Zhou, Modulating electron density of vacancy site by single Au atom for effective CO<sub>2</sub> photoreduction, *Nat. Commun.* 12 (2021) 1675.
- [11] D. Adekoya, M. Tahir, N.A.S. Amin, Recent trends in photocatalytic materials for reduction of carbon dioxide to methanol, *Renew. Sustain. Energy Rev.* 116 (2019), 109389.
- [12] Y. Li, M. Zhang, L. Zhou, S. Yang, Z. Wu, Y. Ma, Recent advances in surface-modified g-C<sub>3</sub>N<sub>4</sub>-based photocatalysts for H<sub>2</sub> production and CO<sub>2</sub> reduction, *Acta Phys.-Chim. Sin.* 37 (2021) 2009030.
- [13] L. Su, P. Wang, X. Ma, J. Wang, S. Zhan, Regulating local electron density of iron single sites by introducing nitrogen vacancies for efficient photo-fenton process, *Angew. Chem. Int. Ed.* 60 (2021) 21261–21266.
- [14] Z. Li, B. Li, Y. Hu, X. Liao, H. Yu, C. Yu, Emerging ultrahigh-density single-atom catalysts for versatile heterogeneous catalysis applications: redefinition, recent progress, and challenges, *Small Struct.* 3 (2022).
- [15] Z.H. Xue, D.Y. Luan, H.B. Zhang, X.W. Lou, Single-atom catalysts for photocatalytic energy conversion, *Joule* 6 (2022) 92–133.
- [16] X.H. Jiang, L.S. Zhang, H.Y. Liu, D.S. Wu, F.Y. Wu, L. Tian, L.L. Liu, J.P. Zou, S. L. Luo, B.B. Chen, Silver single atom in carbon nitride catalyst for highly efficient photocatalytic hydrogen evolution, *Angew. Chem.* 59 (2020) 23112–23116.
- [17] B.B. Sarma, F. Maurer, D.E. Doronkin, J.D. Grunwaldt, Design of single-atom catalysts and tracking their fate using operando and advanced X-ray spectroscopic tools, *Chem. Rev.* 123 (2022) 379–444.
- [18] W. Liu, L. Cao, W. Cheng, Y. Cao, X. Liu, W. Zhang, X. Mou, L. Jin, X. Zheng, W. Che, Q. Liu, T. Yao, S. Wei, Single-site active cobalt-based photocatalyst with a long carrier lifetime for spontaneous overall water splitting, *Angew. Chem.* 56 (2017) 9312–9317.
- [19] Y. Zheng, Y. Jiao, Y. Zhu, Q. Cai, A. Vasileff, L.H. Li, Y. Han, Y. Chen, S.Z. Qiao, Molecule-Level g-C<sub>3</sub>N<sub>4</sub> coordinated transition metals as a new class of electrocatalysts for oxygen electrode reactions, *J. Am. Chem. Soc.* 139 (2017) 3336–3339.
- [20] Y. Zhang, Q. Wang, S. Yang, H. Wang, D. Rao, T. Chen, G. Wang, J. Lu, J. Zhu, S. Wei, X. Zheng, J. Zeng, Tuning the interaction between ruthenium single atoms and the second coordination sphere for efficient nitrogen photofixation, *Adv. Funct. Mater.* 32 (2022) 2112452.
- [21] H. Fei, J. Dong, D. Chen, T. Hu, X. Duan, I. Shakir, Y. Huang, X. Duan, Single atom electrocatalysts supported on graphene or graphene-like carbons, *Chem. Soc. Rev.* 48 (2019) 5207–5241.
- [22] Z. Teng, Q. Zhang, H. Yang, K. Kato, W. Yang, Y.-R. Lu, S. Liu, C. Wang, A. Yamakata, C. Su, B. Liu, T. Ohno, Atomically dispersed antimony on carbon nitride for the artificial photosynthesis of hydrogen peroxide, *Nat. Catal.* 4 (2021) 374–384.
- [23] Y. Li, T. Kong, S. Shen, Artificial photosynthesis with polymeric carbon nitride: When meeting metal nanoparticles, single atoms, and molecular complexes, *Small* 15 (2019), e1900772.
- [24] Q. Wang, K. Liu, K. Hu, C. Cai, H. Li, H. Li, M. Herran, Y.R. Lu, T.S. Chan, C. Ma, J. Fu, S. Zhang, Y. Liang, E. Cortes, M. Liu, Attenuating metal-substrate conjugation in atomically dispersed nickel catalysts for electroreduction of CO<sub>2</sub> to CO, *Nat. Commun.* 13 (2022) 6082.
- [25] X. Shi, Y. Huang, Y. Bo, D. Duan, Z. Wang, J. Cao, G. Zhu, W. Ho, L. Wang, T. Huang, Y. Xiong, Highly selective photocatalytic CO<sub>2</sub> methanation with water vapor on single-atom platinum-decorated defective carbon nitride, *Angew. Chem. Int. Ed.* (2022), e202203063.
- [26] M. Ren, X. Zhang, Y. Liu, G. Yang, L. Qin, J. Meng, Y. Guo, Y. Yang, Interlayer palladium-single-atom-coordinated cyano-group-rich graphitic carbon nitride for enhanced photocatalytic hydrogen production performance, *ACS Catal.* 12 (2022) 5077–5093.
- [27] F. Chen, X.L. Wu, C. Shi, H. Lin, J. Chen, Y. Shi, S. Wang, X. Duan, Molecular engineering toward pyrrole N-rich M-N<sub>4</sub> (M = Cr, Mn, Fe, Co, Cu) single-atom sites for enhanced heterogeneous fenton-like reaction, *Adv. Funct. Mater.* 31 (2021) 2007877.
- [28] T. Wang, J. Chen, X. Ren, J. Zhang, J. Ding, Y. Liu, K. Lim, J. Wang, X. Li, H. Yang, Y. Huang, S. Kawi, B. Liu, Halogen-incorporated Sn catalysts for selective electrochemical CO<sub>2</sub> reduction to formate, *Angew. Chem. Int. Ed.* (2022), e202211174.
- [29] X. Li, S.-G. Han, W. Wu, K. Zhang, B. Chen, S. Zhou, D.-D. Ma, W. Wei, X. Wu, R. Zou, Q.-L. Zhu, Convergent paired electrosynthesis of dimethyl carbonate from carbon dioxide enabled by designing the superstructure of axial oxygen coordinated nickel single-atom catalyst, *Energy Environ. Sci.* (16) (2023) 502–512.
- [30] J. Wang, E. Kim, D.P. Kumar, A.P. Rangappa, Y. Kim, Y. Zhang, T.K. Kim, Highly durable and fully dispersed cobalt diatomic site catalysts for CO<sub>2</sub> photoreduction to CH<sub>4</sub>, *Angew. Chem. Int. Ed.* 134 (2021) e202113044.
- [31] L. Cheng, H. Yin, C. Cai, J. Fan, Q. Xiang, Single Ni atoms anchored on porous few-layer g-C<sub>3</sub>N<sub>4</sub> for photocatalytic CO<sub>2</sub> reduction: the role of edge confinement, *Small* 16 (2020), e2002411.
- [32] R.Y. Zhang, P.H. Li, F. Wang, L.Q. Ye, A. Gaur, Z.A. Huang, Z.Y. Zhao, Y. Bai, Y. Zhou, Atomically dispersed Mo atoms on amorphous g-C<sub>3</sub>N<sub>4</sub> promotes visible-light absorption and charge carriers transfer, *Appl. Catal. B-Environ.* 250 (2019) 273–279.
- [33] X. Liang, N. Fu, S. Yao, Z. Li, Y. Li, The progress and outlook of metal single-atom-site catalysis, *J. Am. Chem. Soc.* 144 (2022) 18155–18174.
- [34] K. Wang, X. Wang, X. Liang, Synthesis of high metal loading single atom catalysts and exploration of the active center structure, *ChemCatChem* 13 (2020) 28–58.
- [35] J. Wu, L. Xiong, B. Zhao, M. Liu, L. Huang, Densely populated single atom catalysts, *Small, Methods* 4 (2019) 1900540.
- [36] S.K. Kaiser, Z. Chen, D. Faust Akl, S. Mitchell, J. Pérez-Ramírez, Single-atom catalysts across the periodic table, *Chem. Rev.* 120 (2020) 11703–11809.
- [37] H. Jin, P. Cui, C. Cao, X. Yu, R. Zhao, D. Ma, W. Song, Understanding the density-dependent activity of Cu single-atom catalyst in the benzene hydroxylation reaction, *ACS, ACS Catal.* (2023) 1316–1325.
- [38] M. Ma, Z. Huang, D.E. Doronkin, W. Fa, Z. Rao, Y. Zou, R. Wang, Y. Zhong, Y. Cao, R. Zhang, Y. Zhou, Ultrahigh surface density of Co-N<sub>2</sub>C single-atom-sites for boosting photocatalytic CO<sub>2</sub> reduction to methanol, *Appl. Catal. B: Environ.* 300 (2022), 120695.
- [39] B. Ravel, M. Newville, Athena, artemis, hephaestus: data analysis for X-ray absorption spectroscopy using IFEFFIT, *J. Synchrotron Radiat.* 12 (2005) 537–541.
- [40] Z.M. Xia, H. Zhang, K.C. Shen, Y.Q. Qu, Z. Jiang, Wavelet analysis of extended X-ray absorption fine structure data: Theory, application, *Phys. B* 542 (2018) 12–19.
- [41] B. Tan, Y. Ye, Z. Huang, L. Ye, M. Ma, Y. Zhou, Promotion of photocatalytic steam reforming of methane over Ag<sup>0</sup>/Ag<sup>+</sup>-SrTiO<sub>3</sub>, *Chin. Chem. Lett.* 31 (2020) 1530–1534.
- [42] M.Z. Ma, J.H. Chen, Z. Huang, W.J. Fa, F. Wang, Y.H. Cao, Y.T. Yang, Z.Q. Rao, R. Wang, R.Y. Zhang, Y.Z. Zou, Y. Zhou, Intermolecular hydrogen bond modulating the selective coupling of protons and CO<sub>2</sub> to CH<sub>4</sub> over nitrogen-doped carbon layers modified cobalt, *Chem. Eng. J.* 444 (2022), 136585.
- [43] M. Ma, Z. Huang, R. Wang, R. Zhang, T. Yang, Z. Rao, W. Fa, F. Zhang, Y. Cao, S. Yu, Y. Zhou, Targeted H<sub>2</sub>O activation to manipulate the selective photocatalytic reduction of CO<sub>2</sub> to CH<sub>3</sub>OH over carbon nitride-supported cobalt sulfide, *Green. Chem.* 24 (2022) 8791–8799.
- [44] R. Fereday, N. Logan, D. Sutton, Anhydrous cobalt (III) nitrate: preparation, spectra, and reactions with some organic ligands, *J. Chem. Soc. A: Inorg., Phys., Theor.* (1969) 2699–2703.
- [45] T. Cseri, S. Békássy, G. Kenessey, G. Liptay, F. Figueras, Characterization of metal nitrates and clay supported metal nitrates by thermal analysis, *Thermochim. Acta* 288 (1996) 137–154.



- [46] L. Kuai, L. Liu, Q. Tao, N. Yu, E. Kan, N. Sun, S. Liu, B. Geng, High-areal density single-atoms/metal oxide nanosheets: a micro-gas blasting synthesis and superior catalytic properties, *Angew. Chem. Int. Ed.* 61 (2022), e202212338.
- [47] Y. Yang, Y. Qian, Z. Luo, H. Li, L. Chen, X. Cao, S. Wei, B. Zhou, Z. Zhang, S. Chen, W. Yan, J. Dong, L. Song, W. Zhang, R. Feng, J. Zhou, K. Du, X. Li, X.M. Zhang, X. Fan, Water induced ultrathin Mo<sub>2</sub>C nanosheets with high-density grain boundaries for enhanced hydrogen evolution, *Nature, Communications* 13 (2022) 7225.
- [48] X. Wang, K. Maeda, A. Thomas, K. Takanebe, G. Xin, J.M. Carlsson, K. Domen, M. Antonietti, A metal-free polymeric photocatalyst for hydrogen production from water under visible light, *Nat. Mater.* 8 (2009) 76–80.
- [49] H. Li, F. Li, J.G. Yu, S.W. Cao, 2D/2D FeNi-LDH/g-C<sub>3</sub>N<sub>4</sub> hybrid photocatalyst for enhanced CO<sub>2</sub> photoreduction, *Acta Phys. -Chim. Sin.* 37 (2021) 2010073.
- [50] Z. Tang, C. Wang, W. He, Y. Wei, Z. Zhao, J. Liu, The Z-scheme g-C<sub>3</sub>N<sub>4</sub>/3DOM-WO<sub>3</sub> photocatalysts with enhanced activity for CO<sub>2</sub> photoreduction into CO, *Chin. Chem. Lett.* 33 (2022) 939–942.
- [51] H. Yu, R. Shi, Y. Zhao, T. Bian, Y. Zhao, C. Zhou, G.I.N. Waterhouse, L.Z. Wu, C. H. Tung, T. Zhang, Alkali-assisted synthesis of nitrogen deficient graphitic carbon nitride with tunable band structures for efficient visible-light-driven hydrogen evolution, *Adv. Mater.* 29 (2017) 1605148.
- [52] Z. Lei, X. Ma, X. Hu, J. Fan, E. Liu, Enhancement of photocatalytic H<sub>2</sub>-evolution kinetics through the dual cocatalyst activity of Ni<sub>2</sub>P-NiS-decorated g-C<sub>3</sub>N<sub>4</sub> heterojunctions, *Acta Phys. -Chim. Sin.* 38 (2022) 2110049.
- [53] H.X. Dai, C.F. Ng, C.T. Au, SrCl<sub>2</sub>-promoted REOx (RE=Ce, Pr, Tb) catalysts for the selective oxidation of ethane: a study on performance and defect structures for ethene formation, *J. Catal.* 199 (2001) 177–192.
- [54] Y. Wang, Y. Qu, B. Qu, L. Bai, Y. Liu, Z.D. Yang, W. Zhang, L. Jing, H. Fu, Construction of six-oxygen-coordinated single Ni sites on g-C<sub>3</sub>N<sub>4</sub> with boron-oxo species for photocatalytic water-activation-induced CO<sub>2</sub> reduction, *Adv. Mater.* 33 (2021), e2105482.
- [55] Y. Zheng, Y. Jiao, Y. Zhu, Q. Cai, A. Vasileff, L.H. Li, Y. Han, Y. Chen, S.Z. Qiao, Molecule-level g-C<sub>3</sub>N<sub>4</sub> coordinated transition metals as a new class of electrocatalysts for oxygen electrode reactions, *J. Am. Chem. Soc.* 139 (2017) 3336–3339.
- [56] Z. Huang, K. Teramura, H. Asakura, S. Hosokawa, T. Tanaka, CO<sub>2</sub> capture, storage, and conversion using a praseodymium-modified Ga<sub>2</sub>O<sub>3</sub> photocatalyst, *J. Mater. Chem. A* 5 (2017) 19351–19357.
- [57] V. Vaiano, M. Matarangolo, O. Sacco, D. Sannino, Photocatalytic treatment of aqueous solutions at high dye concentration using praseodymium-doped ZnO catalysts, *Appl. Catal. B: Environ.* 209 (2017) 621–630.
- [58] C. Liang, C. Liu, F. Li, F. Wu, The effect of Praseodymium on the adsorption and photocatalytic degradation of azo dye in aqueous Pr<sup>3+</sup>-TiO<sub>2</sub> suspension, *Chem. Eng. J.* 147 (2009) 219–225.
- [59] H. Shi, J. Li, H. Wang, J. Hou, K. Li, X. Guo, Chlorine tailored p-d blocks dual-metal atomic catalyst for efficient photocatalytic CO<sub>2</sub> reduction, *Appl. Catal. B: Environ.* 322 (2023), 122139.
- [60] H. Sun, Z. Yan, C. Tian, C. Li, X. Feng, R. Huang, Y. Lan, J. Chen, C.P. Li, Z. Zhang, M. Du, Bixbyite-type Ln<sub>2</sub>O<sub>3</sub> as promoters of metallic Ni for alkaline electrocatalytic hydrogen evolution, *Nat. Commun.* 13 (2022) 3857.
- [61] L.J. Liu, H.L. Zhao, J.M. Andino, Y. Li, Photocatalytic CO<sub>2</sub> reduction with H<sub>2</sub>O on TiO<sub>2</sub> nanocrystals: comparison of anatase, rutile, and brookite polymorphs and exploration of surface chemistry, *ACS Catal.* 2 (2012) 1817–1828.
- [62] C.Q. Han, R.M. Zhang, Y.H. Ye, L. Wang, Z.Y. Ma, F.Y. Su, H.Q. Xie, Y. Zhou, P. K. Wong, L.Q. Ye, Chainmail co-catalyst of NiO shell-encapsulated Ni for improving photocatalytic CO<sub>2</sub> reduction over g-C<sub>3</sub>N<sub>4</sub>, *J. Mater. Chem. A* 7 (2019) 9726–9735.
- [63] M.M. Millet, G. Algara-Siller, S. Wrabetz, A. Mazheika, F. Girgsdies, D. Teschner, F. Seitz, A. Tarasov, S.V. Levchenko, R. Schlögl, E. Frei, Ni single atom catalysts for CO<sub>2</sub> activation, *J. Am. Chem. Soc.* 141 (2019) 2451–2461.
- [64] S. Neatu, J.A. Macia-Agullo, P. Concepcion, H. Garcia, Gold-copper nanoalloys supported on TiO<sub>2</sub> as photocatalysts for CO<sub>2</sub> reduction by water, *J. Am. Chem. Soc.* 136 (2014) 15969–15976.
- [65] N. Ojha, A. Bajpai, S. Kumar, Visible light-driven enhanced CO<sub>2</sub> reduction by water over Cu modified S-doped g-C<sub>3</sub>N<sub>4</sub>, *Catal. Sci. Technol.* 9 (2019) 4598–4613.
- [66] K. Das, R. Das, M. Riyaz, A. Parui, D. Bagchi, A.K. Singh, A.K. Singh, C.P. Vinod, S. C. Peter, Intrinsic Charge Polarization in Bi<sub>19</sub>S<sub>27</sub>Cl<sub>3</sub> Nanorods Promotes Selective C-C Coupling Reaction during Photoreduction of CO<sub>2</sub> to Ethanol, *Adv. Mater.* (2022), e2205994.
- [67] Y.J. Wang, G.L. Zhuang, J.W. Zhang, F. Luo, X. Cheng, F.L. Sun, S.S. Fu, T.B. Lu, Z. M. Zhang, Co-dissolved isostructural polyoxovanadates to construct single-atom-site catalysts for efficient CO<sub>2</sub> photoreduction, *Angew. Chem. Int. Ed.* (2022), e202216592.
- [68] J. Di, X. Zhu, G. Hao, C. Zhu, H. Chen, Q. Liu, R. Duan, H. Hu, Y. Zhang, J. Xiong, R. Long, J. Xia, Y.-X. Weng, W. Jiang, Z. Liu, Vacancy pair-induced charge rebalancing with surface and interfacial dual polarization for CO<sub>2</sub> photoreduction, *ACS Catal.* 12 (2022) 15728–15736.
- [69] Z. Liu, S. Yao, A. Johnston-Peck, W. Xu, J.A. Rodriguez, S.D. Senanayake, Methanol steam reforming over Ni-CeO<sub>2</sub> model and powder catalysts: Pathways to high stability and selectivity for H<sub>2</sub>/CO<sub>2</sub> production, *Catal. Today* 311 (2018) 74–80.
- [70] X. Feng, R. Zheng, C. Gao, W. Wei, J. Peng, R. Wang, S. Yang, W. Zou, X. Wu, Y. Ji, H. Chen, Unlocking bimetallic active sites via a desalination strategy for photocatalytic reduction of atmospheric carbon dioxide, *Nat. Commun.* 13 (2022) 2146.
- [71] S. Yao, B.-Q. Sun, P. Zhang, Z.-Y. Tian, H.-Q. Yin, Z.-M. Zhang, Anchoring ultrafine Cu<sub>2</sub>O nanocluster on PCN for CO<sub>2</sub> photoreduction in water vapor with much improved stability, *Appl. Catal. B: Environ.* 317 (2022), 121702.
- [72] H.T. Yu, Y.M. Xuan, Q.B. Zhu, S. Chang, Highly efficient and stable photocatalytic CO<sub>2</sub> and H<sub>2</sub>O reduction into methanol at lower temperatures through an elaborate gas-liquid-solid interfacial system, *Green. Chem.* 25 (2023) 596–605.